Kinetic Instability of Nanocrystalline Aluminum Prepared by Chemical Synthesis; Facile Room-Temperature Grain Growth

Joel A. Haber and William E. Buhro*

Contribution from the Department of Chemistry, Washington University, St. Louis, Missouri 63130-4899

Received June 5, 1998

Abstract: Nanocrystalline aluminum (*nano*-Al) is synthesized by two chemical methods. Method A consists of the following: reaction of $LiAlH_4$ and $AlCl_3$ at 164 °C in 1,3,5-trimethylbenzene produces *nano*-Al with an average mean coherence length (crystallite size) of 160 ± 50 nm. The byproduct LiCl is removed by washing with MeOH at −25 or 0 °C. Method B consists of the following: *nano*-Al is produced by decomposition of $H_3Al(NMe_2Et)$ under reflux in 1,3,5-trimethylbenzene (ca. 100−164 °C), with or without added decomposition catalyst $Ti(O\text{-}i\text{-}Pr)_4$. Here the mean particle size (40−180 nm) and degree of aggregation of the *nano*-Al depend on the mole percent of decomposition catalyst used (0−1%). The *nano*-Al produced by method A contains 3−4 wt % each of C, O, and Cl; whereas that produced by method B contains only ≤0.25 wt % each of C, O, and Cl and is ≥99 wt % Al. *nano*-Al produced by both methods has been consolidated by uniaxial pressing at 350 MPa for 1 h at 25, 100, or 300 °C. Rapid grain growth is observed at each pressing temperature in method-B powders. The mean grain size doubles at 25 °C within 1 h and continues to increase beyond the nanometer-size regime over longer periods. The low-temperature grain-size instability of the chemically synthesized (method-B) *nano*-Al contrasts markedly with the high-temperature stability (≥300 °C) of *nano*-Al prepared by gas condensation or mechanical attrition. Facile grain growth in the chemically synthesized (method-B) *nano*-Al is attributed to higher grain-boundary purity and to aggregate structures that minimize adventitious oxidation. The results establish that barriers to grain growth in pure *nano*-Al are intrinsically low.

Introduction

We show that the intrinsic barrier to grain (crystallite) growth in nanocrystalline aluminum (*nano*-Al) is low. Our results add to the accumulating evidence that pure nanocrystalline metals are not inherently kinetically stable.[1−8] The kinetic stability often observed likely results from extrinsic origins such as grain-boundary impurities[1,2] rather than from new physical phenomena emerging in ultrafine-grained materials.[9−13] The *nano*-Al we prepared by chemical synthesis has sufficiently low impurity content that intrinsic grain-growth behavior is enabled.

Nanocrystalline metals and ceramics are expected to exhibit improved mechanical properties over conventional coarse-grained materials.[1,2,9−13] Reduction of grain dimensions into the nanometer regime may provide a means to simultaneously strengthen[1,9,10,12,13] and toughen[1,9,12,13] structural materials. In conventional coarse-grained materials having grain dimensions of tens to hundreds of micrometers, increases in strength are generally achieved at the expense of fracture toughness and vice versa.[14] However, predicted changes in deformation and fracture mechanisms should effect increased strength with retention of ductility and toughness (or increased ductility and toughness with retention of strength) in fully dense nanocrystalline materials having grain dimensions of ≤100 nm.[1,9,12,13] These and related expectations have prompted studies of a large number of nanocrystalline ceramics, intermetallics, and metals, with emphasis on how their properties change as a function of grain size.[1,2,9−13]

The predicted property enhancements in nanocrystalline metals have been only partially realized. Nanocrystalline metals have hardnesses that are 2−7 times greater[9] and compressive strengths that are similarly greater[1,17,18] than those of the same coarse-grained metals. However, to date nanocrystalline metals have typically been weak and brittle under tensile loading.[1,9]

(1) Morris, D. G.; Morris, M. A. *Materials Science Forum* **1997**, *235*−*228*, 861−872.
(2) Malow, T. R.; Koch, C. C. *Mater. Sci. Forum* **1996**, *225*−*227*, 595−604.
(3) Günther, B.; Kumpmann, A.; Kunze, H.-D. *Scr. Metall. Mater.* **1992**, *27*, 833−838.
(4) Kumpmann, A.; Günther, B.; Kunze, H.-D. *Mater. Sci. Eng., A* **1993**, *A168*, 165−169.
(5) Gertsman, V. Y.; Birringer, R. *Scr. Metall. Mater.* **1994**, *30*, 577−581.
(6) Lian, J.; Valiev, R. Z.; Baudelet, B. *Acta Metall. Mater.* **1995**, *43*, 4165−4170.
(7) Valiev, R. Z.; Kozlov, E. V.; Ivanov, Yu. F.; Lian, J.; Nazarov, A. A.; Baudelet, B. *Acta Metall. Mater.* **1994**, *42*, 2467−2475.
(8) Akhmadeev, N. A.; Kobelev, N. P.; Mulyukov, R. R.; Soifer, Ya. M.; Valiev, R. Z. *Acta Metall. Mater.* **1993**, *41*, 1041−1046.
(9) Siegel, R. W. *Mater. Sci. Forum* **1997**, *235*−*228*, 851−860.
(10) Gryaznov, V. G.; Trusov, L. I. *Prog. Mater. Sci.* **1993**, *37*, 289−401.
(11) Gleiter, H. *Prog. Mater. Sci.* **1989**, *33*, 223−315.
(12) Siegel, R. W.; Fougere, G. E. *Nanostruct. Mater.* **1995**, *6*, 205−216.
(13) Siegel, R. W.; Fougere, G. E. In *Nanophase Materials, Synthesis, Properties, Applications*; Hadjipanayis, G. C., Siegel, R. W., Eds.; NATO ASI Series, Vol. 260; Kluwer Academic: Dordrecht, 1994; pp 233−261.
(14) Strength and fracture toughness in conventional materials depend largely on dislocation mobility. Dislocations are immobile in strong, brittle materials such as ceramics. Dislocations are very mobile in ductile, soft but tough metals. Chemical or microstructural changes that limit dislocation mobility strengthen but embrittle metals.[12,13,15,16]
(15) Gordon, J. E. *The New Science of Strong Materials*, 2nd ed.; Princeton University Press: Princeton, 1988; pp 91−98, 117, 209−230.
(16) Geselbracht, M. J.; Ellis, A. B.; Penn, R. L.; Lisensky, G. C.; Stone, D. S. *J. Chem. Educ.* **1994**, *71*, 254−261.

10.1021/ja981972y CCC: $15.00
Published on Web 10/13/1998

Neither hardness nor compressive strength is very sensitive to the porosity or other internal flaws present in nanocrystalline consolidates. Most nanocrystalline consolidates are obtained by compaction of fine powders consisting of nanometer-sized crystallites in micrometer-sized aggregates, which resist consolidation to full density. Densities of only 75−95% of theoretical values are typically achieved; considerable nano- and microporosity remain.[1] Tensile strength, ductility, and fracture toughness *are* sensitive to porosity and related flaws. Therefore, improvements in consolidation or other means of reducing residual porosity are required to allow the ductility and fracture-toughness expectations to be properly tested.[1] Elucidation of the mechanisms governing hardening, plastic deformation, fracture, and microstructural stability of nanostructured materials continues to be an active research area of fundamental importance.[1,2,9,10,11,19]

Retention of properties due to nanoscale grains requires grain-size stability. Nanocrystalline materials are *thermodynamically* unstable because large fractions of the constituent atoms reside in (high-energy) grain boundaries.[10,11,20−22] Grain growth, which decreases grain-boundary volume, decreases total free energy substantially. However, most nanocrystalline metals and ceramics behave as though they are deeply metastable and resist grain growth to high temperatures.[10,11] At issue is whether high barriers to grain growth are intrinsic[12,13,20,21] or extrinsic[1,2,22] in origin. Solute or impurity segregation at grain boundaries, grain-boundary pinning by additive or impurity (second-phase) particles (Zener drag[23]), and pores are effective impediments to grain growth.[1,2] Recent observations of low-temperature grain growth in nanocrystalline copper,[3−8] silver,[3,4] and palladium[3,4] suggest that *intrinsic* barriers to grain growth in nanocrystalline metals are actually low.

Nanocrystalline aluminum has presented a dramatic counterexample to the facile coarsening found in nanocrystalline copper, silver, and palladium.[24] Samples produced by inert-gas condensation[26−31] and mechanical attrition (high-energy ball milling)[31−35] undergo minimal grain growth during consolidation and thermal processing.[27−31] In some cases the ultrafine-grained microstructure is retained after melting.[30,31]

However, as described herein the *nano*-Al prepared by chemical synthesis undergoes rapid coarsening upon room-temperature consolidation. We attribute the facile grain growth to the purity of the chemically produced powders and to favorable aggregate structures that protect nanocrystallite surfaces from adventitious oxidation. To our knowledge, this work constitutes the first isolation of *nano*-Al from chemical syntheses.[36,37]

Results

Preparative Method A. Reduction of $AlCl_3$ with $LiAlH_4$ afforded *nano*-Al according to eq 1. The *nano*-Al was obtained

$$3LiAlH_4 + AlCl_3 \xrightarrow[164\ ^\circ C]{1,3,5\text{-}Me_3C_6H_3} 4\textit{nano}\text{-}Al + 3LiCl + 6H_2 \quad (1)$$

as a mixture with the LiCl byproduct, which was removed by extraction with cold (0 °C) MeOH. We succeeded in extracting up to 2.5 g of the mixture in a single operation, provided that the temperature was maintained between −25 and 0 °C. However, attempts to extract larger quantities resulted in runaway exothermic oxidation of *nano*-Al by MeOH. Consequently, method A (eq 1) was inconvenient for production of large quantities of *nano*-Al. Additionally, the *nano*-Al contained significant amounts of C, O, and Cl as determined by analysis of a pellet consolidated from method-A powder (see below).

We surmised that eq 1 proceeded by the intermediate formation and decomposition of alane, AlH_3. Alane may be isolated as an Et_2O adduct from reactions of $LiAlH_4$ and $AlCl_3$ (as in eq 1) in Et_2O near room temperature.[38,39] Stable alane−amine adducts have been prepared similarly.[40] We expected that LiCl-free *nano*-Al would be produced by decomposition of an appropriate, purified alane adduct, $H_3Al(L)$. The adduct $H_3Al(NMe_2Et)$ was selected for study because it has proven convenient for the chemical vapor deposition of Al films at ≥100 °C.[41]

Preparative Method B. $H_3Al(NMe_2Et)$ was prepared by the method of Frigo and co-workers.[40] We found that $H_3Al(NMe_2Et)$ decomposed under reflux in 1,3,5-trimethylbenzene solution with or without added decomposition catalyst[39] $Ti(O\text{-}i\text{-}Pr)_4$ according to eq 2. In the absence of $Ti(O\text{-}i\text{-}Pr)_4$ decomposition

$$H_3Al(NMe_2Et) \xrightarrow[\substack{\text{w/ or w/o cat.}\\ Ti(O\text{-}i\text{-}Pr)_4\\ \leq 164\ ^\circ C}]{1,3,5\text{-}Me_3C_6H_3} \textit{nano}\text{-}Al + {}^3/_2H_2 + NMe_2Et \quad (2)$$

(17) Suryanarayanan, R.; Frey, C. A.; Sastry, S. M. L.; Waller, B. E.; Buhro, W. E. In *Processing and Properties of Nanocrystalline Materials*; Suryanarayana, C., Singh, J., Froes, F. H., Eds.; Minerals, Metals and Materials Society: Warrendale, PA, 1996; pp 407−413.
(18) Suryanarayanan, R.; Frey, C. A.; Sastry, S. M. L.; Waller, B. E.; Bates, S. E.; Buhro, W. E. *J. Mater. Res.* **1996**, *11*, 439−448.
(19) Schiøtz, J.; Di Tolla, F. D.; Jacobsen, K. W. *Nature* **1998**, *391*, 561−563.
(20) Rivier, N. In *Physics and Chemistry of Finite Systems: From Clusters to Crystals*; Jena, P., Khanna, S. N., Rao, B. K., Eds.; Kluwer Academic: Dordrecht, 1992; pp 189−198.
(21) Fecht, H. J. *Phys. Rev. Lett.* **1990**, *65*, 610−613.
(22) Gärtner, F.; Bormann, R.; Birringer, R.; Tschöpe, A. *Scr. Metall. Mater.* **1996**, *35*, 805−810.
(23) Morris, D. G.; Morris, M. A. *Mater. Sci. Eng., A* **1991**, *A134*, 1418−1421.
(24) Birringer indicated in a review[25] that nanocrystalline aluminum underwent grain growth at room temperature, but to our knowledge, the experiments upon which that conclusion was based have not been described. Our current results agree with Birringer's indication.
(25) Birringer, R. *Mater. Sci. Eng., A* **1989**, *A117*, 33−43.
(26) Hahn, H.; Averback, R. S. *J. Appl. Phys.* **1990**, *67(2)*, 1113−1115.
(27) Gutmanas, E. Y.; Trusov, L. I.; Gotman, I. *Nanostruct. Mater.* **1994**, *4*, 893−901.
(28) Qin, X. Y.; Wu, X. J.; Cheng, L. F. *Nanostruct. Mater.* **1993**, *2*, 99−108.
(29) Würschum, R.; Greiner, W.; Schaefer, H.-E. *Nanostruct. Mater.* **1993**, *2*, 55−62.
(30) Sánchez-López, J. C.; Fernández, A.; Conde, C. F.; Morant, C.; Sanz, J. M. *Nanostruct. Mater.* **1996**, *7*, 813−822.
(31) Eckert, J.; Holzer, J. C.; Ahn, C. C.; Fu, Z.; Johnson, W. L. *Nanostruct. Mater.* **1993**, *2*, 407−413.
(32) Eckert, J.; Holzer, J. C.; Krill, J. C., III.; Johnson, W. L. *J. Mater. Res.* **1992**, *7*, 1751−1761.
(33) Al Sadi, A.; Bonetti, E.; Mattioli, P.; Valdrè, G. *J. Alloys Compd.* **1994**, *211/212*, 489−493.
(34) Bonetti, E.; Scipione, G.; Valdrè, G.; Enzo, S.; Frattini, R.; Macrì, P. P. *J. Mater. Sci.* **1995**, *30*, 2220−2226.
(35) Oleszak, D.; Shingu, P. H. *J. Appl. Phys.* **1996**, *79*, 2975−2980.
(36) Rieke, R. D.; Chao, L. *Synth. React. Inorg. Met.-Org. Chem.* **1974**, *4*, 101.
(37) Tsai, K.-L.; Dye, J. L. *J. Am. Chem. Soc.* **1991**, *113*, 1650−1652.
(38) Finholt, A. E.; Bond, A. C.; Schlesinger, H. I. *J. Am. Chem. Soc.* **1947**, *69*, 1199−1203.
(39) Brower, F. M.; Matzek, N. E.; Reigler, P. F.; Rinn, H. W.; Roberts, C. B.; Schmidt, D. L.; Snover, J. A.; Terada, K. *J. Am. Chem. Soc.* **1976**, *98*, 2450−2453.
(40) Frigo, D. M.; van Eijden, G. J. M.; Reuvers, P. J.; Smit, C. J. *Chem. Mater.* **1994**, *6*, 190−195.
(41) Simmonds, M. G.; Phillips, E. C.; Hwang, J.-I.; Gladfelter, W. L. *Chemtronics* **1991**, *5*, 155−158.

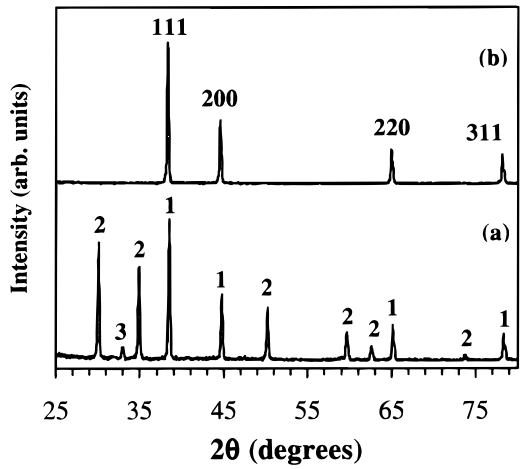

Figure 1. XRD patterns of method-A powders. (a) As precipitated: (1) *nano*-Al, (2) LiCl, (3) LiCl·H_2O. (b) After MeOH wash; *nano*-Al reflections are labeled by their Miller indices, *hkl*.

of $H_3Al(NMe_2Et)$ occurred at ca. 164 °C. The resulting *nano*-Al was obtained as a spongy mass coating the bottom of the reaction vessel, which could be ground in a mortar and pestle into coarse flakes. In the presence of catalytic amounts of Ti(O-*i*-Pr)$_4$, decomposition of $H_3Al(NMe_2Et)$ occurred well below 164 °C, and the *nano*-Al was precipitated as a powder. The spongy and powder forms of the product suggested that the decomposition occurred upon the heated vessel surface without added catalyst and in solution dispersion with added catalyst. The purity of method-B powder was considerably greater than the purity of method-A powder (see below).

Characterization of *nano*-Al Produced by Method A. An X-ray powder diffraction (XRD) pattern of the eq 1 product prior to extraction contained reflections for LiCl and *nano*-Al (Figure 1a). After MeOH extraction of the powder, *nano*-Al was the only crystalline phase detected (Figure 1b), indicating that the C-,O-, and Cl-containing impurities present were poorly crystalline or in amounts below the (few %) XRD detection limit. The mean coherence length determined by Scherrer analysis of XRD line widths (see the Experimental Section) varied from trial to trial over the range of 90 to >200 nm. We were unable to identify the reaction parameter responsible for this large variation. The average in the mean coherence length was 160 ± 50 nm over sixteen trials, establishing Al crystallite sizes of that approximate magnitude and size distribution.

Microscopic investigation of the method-A powder revealed aggregates of small Al crystallites and larger nonaggregated polyhedral Al crystallites. Scanning electron microscopy (SEM) images established a powder microstructure consisting mainly of particle aggregates having dimensions of 3−150 μm. These large aggregates were partially dismantled and suspended in pyridine in an ultrasonic cleaning bath. Transmission electron microscopy (TEM) images of the suspended material showed smaller residual aggregates of faceted (Figure 2a) and rounded (Figure 2b) particles. The dimensions of the particles were consistent with the mean XRD coherence length (160 ± 50 nm, Figure 2b). The TEM images also consistently revealed minority fractions of nonaggregated polyhedral crystallites including tetrahedra, octahedra, and cubooctahedra (Figure 3). Although the method-A powders contained broad distributions of particle sizes as evidenced by Figures 2 and 3, individual aggregates tended to contain similarly sized particles.

Characterization of *nano*-Al Produced by Method B. The crystallite sizes, estimated by mean XRD coherence lengths, and the degree of aggregation of the *nano*-Al produced by eq 2 depended upon the amount of Ti(O-*i*-Pr)$_4$ decomposition catalyst used (see Table 1 and Figure 4). When no catalyst was added, the mean coherence lengths were 44−82 nm. Addition of 0.01 mol % of Ti(O-*i*-Pr)$_4$ catalyst caused the mean coherence length to increase to 197 nm. The mean coherence length then decreased with increasing amount of catalyst to 50−75 nm at 1 mol % catalyst (Table 1 and Figure 4). The initial jump in the *nano*-Al coherence length with added catalyst was ascribed to the change in the mechanism of $H_3Al(NMe_2Et)$ decomposition noted previously. The decrease in coherence length with increasing amount of catalyst was ascribed to an increasing crystallite nucleation rate.

In general, with decreasing size the particles adopted non-faceted morphologies and, as expected,[31] formed larger, more densely packed aggregates. The large flakes produced by grinding the spongy eq 2 product obtained without added catalyst consisted of dense aggregates 1−2 μm in diameter with nanosized features and loose aggregates of rounded nanometer-sized particles (Figure 5a). As above, the aggregates were partially dismantled by sonication in pyridine. TEM images

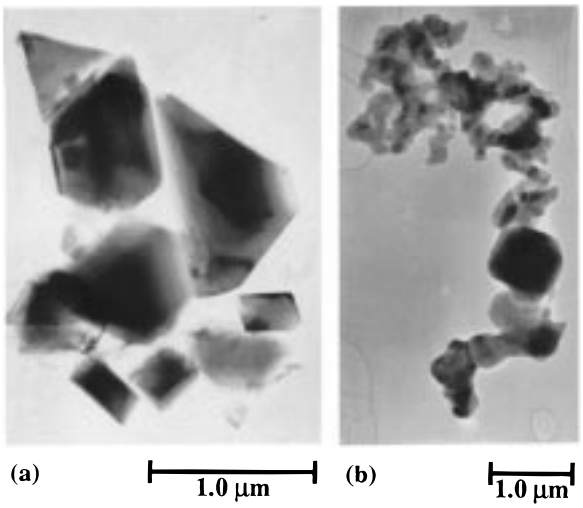

Figure 2. Aggregates of the two types found in method-A *nano*-Al powders: (a) larger faceted crystallites from a sample having an XRD coherence length of ∼200 nm; (b) smaller rounded crystallites from a sample having an XRD coherence length of ∼100 nm.

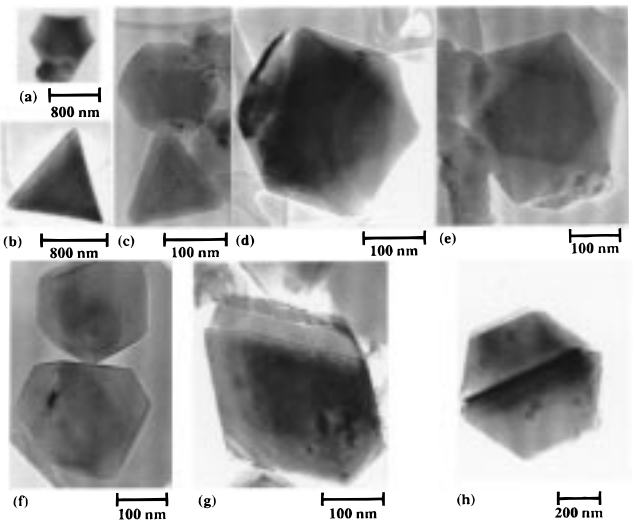

Figure 3. Nonaggregated polyhedral crystallites found as a minor fraction in method-A and method-B *nano*-Al powders: (a) and (h) cubooctahedra, (b) tetrahedron, (c) tetrahedron and cuboctahedron with rounded edges, (d) and (e) octahedra, (f) and (g) other polyhedra.

Table 1. Mean Coherence Lengths of *Nano*-Al Prepared by Method B

powder	concentration of $H_3Al(NMe_2Et)$[a]	mol % Ti(O-*i*-Pr)$_4$[b]	Scherrer (XRD) coherence length[c] (nm)
B1	2	0	45 ± 3
B2	2.4	0	67 ± 4
B3	2.4	0	82 ± 20
B4	2.5	0	48 ± 2
B5	2.0−2.4	0.0035−0.014	197 ± 20
B6	1	0.07−0.14	128 ± 11
B7	3.2−4.0	0.16	116 ± 10
B8	2.4	0.17	97 ± 7
B9	2.6	0.18	128 ± 1
B10	2.4	0.20	95 ± 8
B11	2.6	0.29	108 ± 5
B12	1.6−2.1	0.41	73 ± 7
B13	2.5−3.0	0.58	48 ± 8
B14	2.5−3.0	0.51−0.67	62 ± 11
B15	2.4	0.64	74 ± 4
B16	2.4	0.71	50 ± 10
B17	2.5	0.97	62 ± 6
B18	1.6−2.1	1.15	99 ± 16

[a] Moles of $H_3Al(NMe_2Et)$ per L of 1,3,5-trimethylbenzene. [b] On the basis of $H_3Al(NMe_2Et)$. [c] Coherence lengths and errors were extracted from the XRD data as described in the Experimental Section. Size and strain contributions to the XRD line widths were deconvoluted using the method applied to the data from consolidated pellets (see the Experimental Section), but the resulting sizes were within the error limits of the simple Scherrer values recorded here, indicating that strain contributions were negligible.

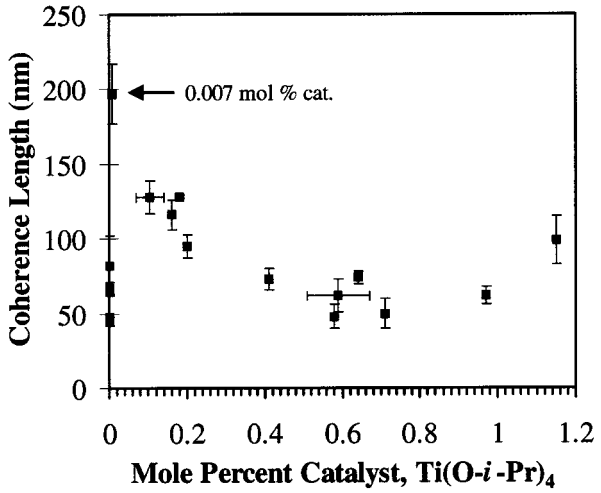

Figure 4. Dependence of the XRD coherence length (a measure of mean crystallite size) in method-B *nano*-Al powders upon the quantity of Ti(O-*i*-Pr)$_4$ catalyst used in eq 2.

(Figure 5b) of the suspended fraction revealed that the tight aggregates were composed of 20−50 nm crystallites, consistent with the XRD coherence length.

In contrast, the eq 2 products with the largest mean coherence lengths, those produced using up to 0.29 mol % of catalyst, were the finest powders and frequently passed through medium porosity glass frits. SEM images (Figure 5c) indicated that these fine powders consisted largely of faceted crystallites 150−500 nm in diameter. A minority fraction of 0.5−1.5 μm aggregates having 20−50 nanometer-sized rounded features was also present. TEM images (Figure 5d) of sonicated, suspended material showed that the faceted crystallites were readily dispersed and that the tight aggregates again consisted of 20−50 nm diameter crystallites.

When greater than 0.41 mol % of catalyst was used in eq 2, dense aggregates were again formed (Figure 5e, g), similar to those from the catalyst-free eq 2 synthesis (Figure 5a). The

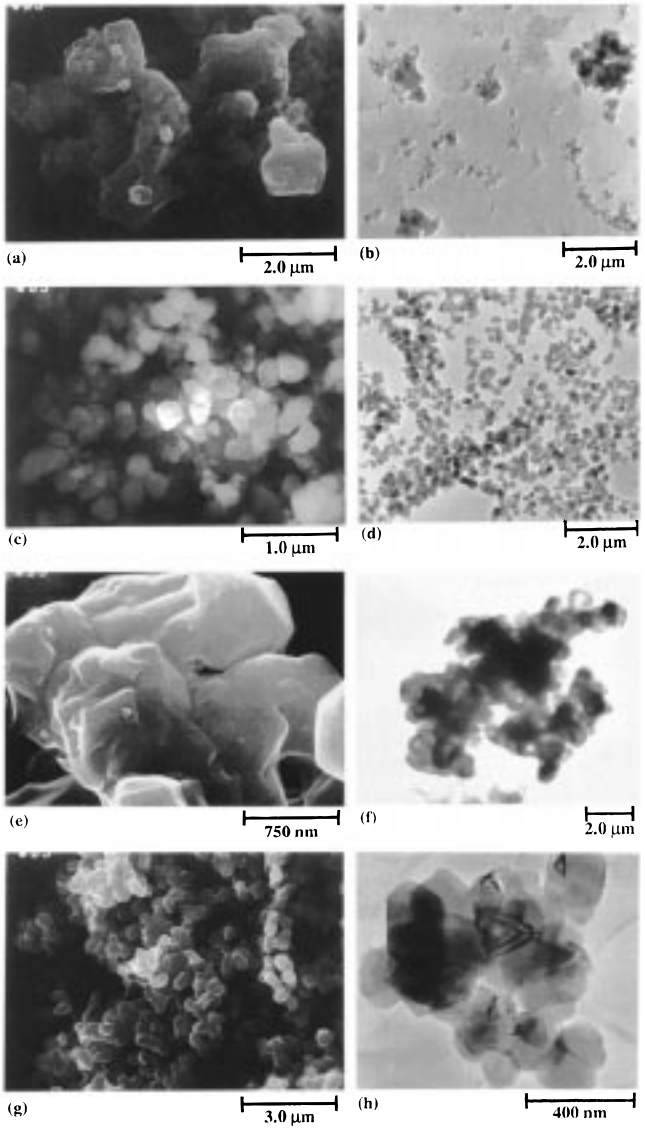

Figure 5. SEM (left) and TEM (right) images of method-B *nano*-Al powders. From samples prepared by eq 2 using: (a) and (b) 0 mol %, (c) and (d) 0.007−0.29 mol %, (e) and (f) 0.64 mol %, and (g) and (h) 0.71 mol % Ti(O-*i*-Pr)$_4$ catalyst.

larger particles (1.0−2.0 μm in diameter) making up these aggregates were polycrystallites that in some cases exhibited partially formed facets. The internal structure (polycrystallinity) of the particles was established by TEM images of sonicated, suspended samples (Figure 5f, h); tightly aggregated primary crystallites sharing angular interfaces were evident (Figure 5h). The primary crystallite sizes in Figure 5h are 50−200 nm.

The facets observed upon some of the aggregates (such as in Figure 5e) likely indicate the onset of recrystallization and grain growth within them. The faceted constituents of the aggregates resemble the previously discussed polyhedral *single* crystallites (Figure 3) obtained as minor product fractions in both method A and B syntheses, suggesting that clearly observable facets emerge only in larger crystallites having dimensions of approximately ≥200 nm.

Characterization of Consolidated *nano*-Al. Pellets were consolidated by uniaxial pressing for 1 h at 350 MPa and 25, 100, or 300 °C. The pressing was conducted in a hot press assembled in an argon-filled glovebox to minimize adventitious oxidation associated with powder transfers and die loading. The pellets produced from both method-A and method-B powders

Table 2. Properties of Consolidated *nano*-Al

pellet[a]	pellet mass (g)	T_r[b]	% density[c]	mean grain size[d] (nm)	rms strain[e] (10^{-4})	microhardness (MPa)
A-100	1.27	0.40	84	270 ± 160	3.6 (± 120%)	410 ± 20
A-300	0.77	0.61	89	190 ± 50	2.1 (±110%)	550 ± 60
B13−100	3.53	0.40	90	>335		470 ± 14
B15−RT	0.75	0.32	75	153 ± 14	3.8 (±30%)	560 ± 50
B15−100	0.79	0.40	88	168 ± 24	3.0 (±50%)	570 ± 40
B15−300	0.75	0.61	95	200 ± 16	2.9 (±25%)	760 ± 50

[a] The pellet label combines the powder synthesis method (and run), and the pressing temperature (in °C). [b] Reduced pressing temperature, T_r, is the absolute pressing temperature divided by the absolute melting temperature of bulk Al; the reduced recrystallization temperature of bulk Al is 0.54.[32] [c] On the basis of the density of bulk Al; we estimate a 3% error in these geometrically determined values. [d] Grain sizes and errors were determined from XRD line widths according to eq 3 and as described in the Experimental Section. In one case, grain size was estimated as greater than the coherence length for the least strain-broadened reflection, the 111. [e] Strains were determined from XRD line widths as described in the Experimental Section.

were polished, without disintegration, to a metallic luster, indicating at least moderate interparticle bonding. The density, mean grain size, rms strain, and microhardness of several pellets are given in Table 2. (Pellets were labeled according to the source of the powder and the pressing temperature. Thus, pellet B15-25 was pressed from method-B run-15 powder, see Table 1, at 25 °C.) As described below, density, porosity, and microhardness appeared to correlate with the purity of the starting *nano*-Al powder and the pressing temperature. The most significant result was the observation of grain growth upon consolidation of the pellets, even at room temperature (see below).

Elemental analysis performed by glow-discharge mass spectrometry on portions of the pellets A-300 and B13-100 established that the *nano*-Al produced by method B was purer by an order of magnitude than that produced by method A. Pellet A-300 was only 87.0 wt % Al and contained 3.0, 4.0, and 3.3 wt % of C, O, and Cl, respectively. Pellet B13-100 was 99 wt % Al and contained only 0.23, 0.25, 0.14, and 0.32 wt % of C, O, Cl, and Ti, respectively. Pellet A-300 contained 0.12 wt % of Li, in significant molar deficiency relative to the residual Cl. Thus, the Cl present was not due to substantial amounts of residual LiCl, but more likely to unreacted $AlCl_3$. Energy-dispersive X-ray spectroscopy (EDS) conducted in the SEM on pellets A-100 and A-300 gave compositional data consistent with those from glow-discharge mass spectrometry. Furthermore, EDS on these samples established that Cl was distributed heterogeneously, and in polished specimens that the Cl and O impurities were concentrated near cracks and pores. Small amounts (<0.3 atom %) of heterogeneously distributed Si were also detected, which presumably derived from glass surfaces, fritted disks, or silicone grease applied to stopcocks. EDS of B15-25, B15-100, and B15-300 gave compositional data consistent with those from glow-discharge mass spectrometry on B13-100, except that Ti and O were present in slightly greater amounts, possibly in part because of the slightly larger mol % of Ti(O-*i*-Pr)$_4$ used in the synthesis of the B15 powder. Only 30 to 50% of the Ti added in the catalyst was incorporated into the *nano*-Al product; the rest of the Ti presumably remained soluble and was removed in the washing step. The greater purity of the method-B powders, revealed by analyses of the consolidated pellets, was presumably due to the absence of Cl in the method-B, $H_3Al(NMe_2Et)$ precursor and the omission of the MeOH wash used in the method-A synthesis.

Pellet densities were measured at 75−95% of the theoretical Al density (Table 2), and scaled roughly with powder purity and pressing temperature. Pellets pressed from method-A powders were less dense than those pressed from method-B powders under the same conditions. The observed density range was typical of consolidated nanocrystalline materials.[1,2,9−11] The lower densities of method-A pellets may have been due to inhibition of densification by impurity phases.

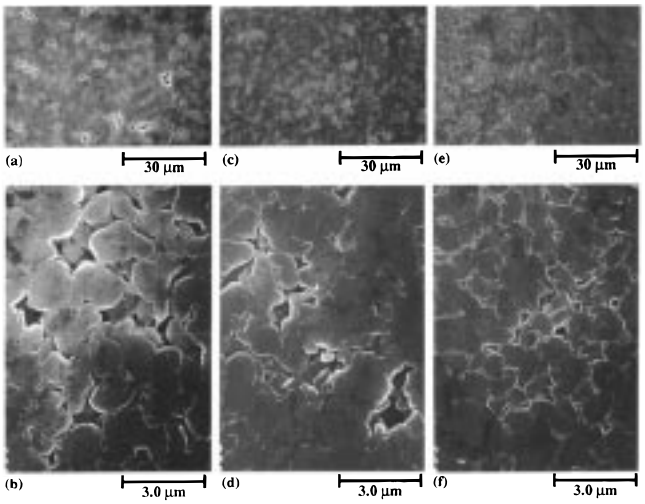

Figure 6. SEM images at two magnifications of unpolished, air-unexposed surfaces of pellets pressed from powder B15 (see Tables 1 and 2). Pressing temperature: (a) and (b) 25 °C, (c) and (d) 100 °C, and (e) and (f) 300 °C. Note that the highest pressing temperature removed micrometer-sized pores, but not nanometer-sized pores.

SEM images of *unpolished* pellet surfaces showed that porosity scaled with density. Pore sizes ranged from 5 μm to < 500 nm in diameter. Pellet A-100 contained extensive μm-scale porosity, whereas the denser pellet A-300 contained only nanometer-scale pores. The pellets pressed from powder B15 showed the same trend (see Figure 6). Pellet B15-300 retained some nanometer-scale porosity; thus, even the higher-purity pellets pressed at relatively high temperature were not fully dense. SEM images confirmed the trend in the geometrically determined densities.

SEM images of *polished* pellet surfaces gave misleading estimations of porosity. Polishing greatly increased the apparent porosity by increasing the number of submicrometer-scale pores observed. The polished pellets appeared to contain 30−50% porosity by optical microscopy (metallography), which were values inconsistent with the geometrically determined densities. We believe that this apparent porosity increase resulted from removal of particles and aggregates from the surface during polishing and from reaction of the incompletely densified *nano*-Al with the water used in polishing. Thus, the polishing media used in conventional polishing techniques are not ideal for incompletely densified, reactive nanostructured materials.

The Vickers microhardnesses of the pellets scaled roughly with density (Table 2) and were greater than the microhardness of pure, coarse-grained Al (290 MPa).[32] Our microhardnesses (410−760 MPa) were less than that of sintered aluminum

powder (1450 MPa),[27] which contains a large volume fraction of oxides, and less than the previously reported microhardness of *nano*-Al (120-nm grain size) prepared by gas-phase condensation (1700 MPa).[27] Because of the ease of measurement, microhardness is often used as an approximate indicator of strength in nanocrystalline materials. However, microhardness and tensile strength respond differently to flaw content and the degree of interparticle bonding. Many factors including grain size, grain-boundary structure, porosity, and impurity-derived dispersoid populations influence microhardness.[1] Therefore, differences in microhardness among conventional aluminum, sintered aluminum powder, and fine-grained aluminum are not readily interpretable. We may not conclude that the somewhat enhanced microhardnesses of our samples were due to small grain sizes.

Grain Growth in Consolidated *nano*-Al. During consolidation the *nano*-Al grain sizes grew beyond the nanocrystalline size regime (to 150 to >330 nm; see Table 2). Substantial grain growth was most evident in the pellets pressed from method-B powders because of their smaller initial particle sizes and likely also because of their greater purities, as compared to the method-A powders. The mean grain size more than doubled in pellet B15-25, pressed at room temperature, and increased by factors of 3−4 in some method-B pellets pressed at higher temperatures. The large uncertainties in the final grain size for the larger-grained consolidates (Table 2) were due to increasingly narrowed XRD line widths, which failed to provide precise measures of grain size for grains larger than ca. 200 nm, and to crystallite-shape anisotropies, which were not accounted for by our analytical model (see the Experimental Section). The rms microstrains of $2-4 \times 10^{-4}$, also extracted from XRD line widths (see the Experimental Section), were much less than the maximal rms microstrains of 2×10^{-3} obtained by mechanical attrition of aluminum,[31] indicating that the *nano*-Al was only moderately strained as a result of consolidation.

Grain sizes continued to increase when the pellets were stored at room temperature as evidenced by further narrowing of XRD line widths. After three months, XRD analyses of pellets B15-25, B15-100, and B15-300 indicated that grain sizes had surpassed 200 nm, and were thus outside the regime for accurate grain-size measurement by XRD. Pellet B15-300 was selected for TEM analysis because it was the densest and best able to survive slicing, polishing, and ion milling. TEM images (Figure 7) of the thinned specimen revealed enlarged grains. Irregular crystallite shapes and contrast prevented a detailed statistical analysis of the grain-size distribution, but the mean grain size appeared to be ≥300 nm with several single-crystalline regions of ca. 1 μm in diameter also evident. Thus, the mean grain size was found to be larger than that determined by XRD immediately after consolidation, confirming continued grain growth.

Because of the grain growth that occurred during and after pressing, the consolidated pellets were not nanocrystalline. The incompletely densified pellets were embrittled by the submicrometer porosity retained and were therefore unsuitable for measurement of tensile properties. Although the pellets could have been pressed at higher temperatures or pressures to attempt the removal of residual porosity, grain growth beyond the nanometer size regime had already occurred. Thus, our chemical synthesis of *nano*-Al followed by compaction apparently cannot produce fully dense, *pure* nanocrystalline Al. If facile room-temperature grain growth is an intrinsic characteristic of pure nanocrystalline Al, as our results suggest, then fully dense, pure nanocrystalline Al is not practicably achievable.

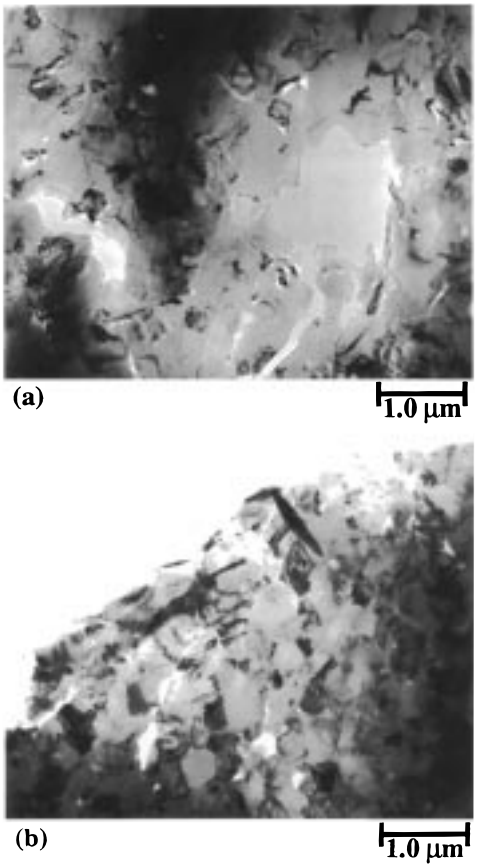

Figure 7. TEM images from a sliced and thinned specimen from pellet B15-300 (see Table 2) after the pellet aged for 3 months at room temperature. Note the presence of many grains with ca. 1-μm dimensions, and the near absence of grains having ≤100-nm dimensions.

Discussion

Grain growth occurs significantly faster and at lower temperatures in the chemically synthesized (method-B) *nano*-Al described here than in *nano*-Al prepared by gas condensation or mechanical attrition.[23] The kinetic stability of nanocrystalline metals has been previously attributed to small grain sizes and, more precisely, to narrow grain-size distributions.[12,13,20] However, we argue below that such stability is likely due to extrinsic impurities. Enhanced grain growth in the chemically synthesized (method-B) *nano*-Al is likely due to greater grain-boundary purity and the arrangement of nanocrystallites into favorable aggregate structures.

Whereas we report grain-size doubling at 25 °C for chemically synthesized (method-B) *nano*-Al, previous studies reported no or minimal grain growth up to temperatures of 300,[27] 330,[28] or 800 °C[31] for *nano*-Al prepared by the other methods. Annealing at 610 °C was required to double grain sizes in *nano*-Al produced by gas condensation.[28] Apparently, one or more of the factors that stabilize nanometer-scale grain structures is lacking in the chemically synthesized *nano*-Al. Grain-size distribution may be eliminated as a likely factor.

Rivier proposed that nanocrystalline materials are kinetically stabilized by narrow grain-size distributions.[20] According to this model, the local driving force for grain coarsening is the difference in chemical potential between neighboring grains. Chemical potential is grain-size dependent, such that a smaller grain would be readily consumed to enlarge an already larger neighboring grain. However, neighboring grains of the same size are trapped in a metastable equilibrium without sufficient

driving force to enlarge one at the expense of the other. If this is the origin of increased grain-size stability in *nano*-Al prepared by gas condensation or mechanical attrition, then we should observe significantly broader grain-size distributions in our samples than were observed in the former.

However, the grain-size distributions achieved in the gas-condensation and mechanical-attrition syntheses are fairly broad and not markedly narrower than those achieved in the chemical syntheses. A statistical analysis from TEM images of *nano*-Al prepared by gas condensation gave a grain-size distribution of 10−60 nm (30 nm ± 100%).[30] Microscopic images of samples prepared in other gas-condensation[27] and mechanical-attrition syntheses reveal similar and broader size distributions.[32,33] As established above, the method-B powders subjected to consolidation possessed grain-size distributions of 20−200 nm, and mean crystallite sizes of 48 and 74 nm (for samples B13 and B15, respectively; see Table 1). These distributions are shifted to slightly larger mean sizes than those achieved by gas condensation and mechanical attrition and are asymmetric, possessing a minority fraction of larger crystallites in the size range of 100−200 nm. However, the relative magnitudes of the size distributions from the chemical syntheses, relative to the midpoint of the observed size ranges, are comparable to those from gas condensation and mechanical attrition. Consequently, the Rivier model[20] does not account for the differing grain-size stabilities of *nano*-Al prepared by the various methods. The validity of the model is neither supported nor refuted, but the model does not distinguish the present comparison. Presumably, none of the *nano*-Al samples have sufficiently narrow grain-size distributions to be stabilized by Rivier's proposed effect.

The high grain-size stability of *nano*-Al prepared by gas condensation or mechanical attrition, in some cases to temperatures above the melting point of bulk Al (660 °C),[31] exceeds reasonable expectation for pure *nano*-Al. Stabilities for nanocrystalline phases should scale roughly with melting points and recrystallization temperatures for the bulk phases. Gleiter[11] and Birringer[25] stated that 10-nm grains in metals having bulk melting points of about 600 °C or less double within 24 h at room temperature (e.g., Sn, Pb, Al,[24] or Mg). Nanocrystalline metals with higher bulk melting points have higher grain-size stability. Nanocrystalline Cu (bulk T_m = 1083 °C) is stable to ≤100 °C, nanocrystalline Pd (bulk T_m = 1552 °C) to ≤150 °C, and nanocrystalline Fe (bulk T_m = 1535 °C) to ≤200 °C.[11,25] The recrystallization temperature of coarse-grained (bulk) Al is only 80 °C.[32] Because Al is one of the lowest-melting fcc metals, *nano*-Al should exhibit *less* resistance to grain growth than do other nanocrystalline metals but, apart from the present findings, has instead exhibited *more*.

This unexpected resistance to grain growth suggests extrinsic stability origins. Indeed, *nano*-Al prepared by gas condensation and oxidatively passivated with 4-nm aluminum-oxide coating layers retained 30-nm grain sizes after heating to 725 °C.[30,44] In a separate study, Al nanocrystallites prepared by gas condensation were found to be adventitiously coated with 6-nm aluminum-oxide layers, to which was attributed the grain-size stability of the sample at 800 °C.[31] Second phases (impurities) at grain boundaries are known to inhibit coarsening in nanocrystalline materials.[1,2,23] Consequently, grain-boundary oxide impurities, usually adventitious and unrecognized, are implicated as the extrinsic origin of stability in *nano*-Al prepared by gas condensation or mechanical attrition.

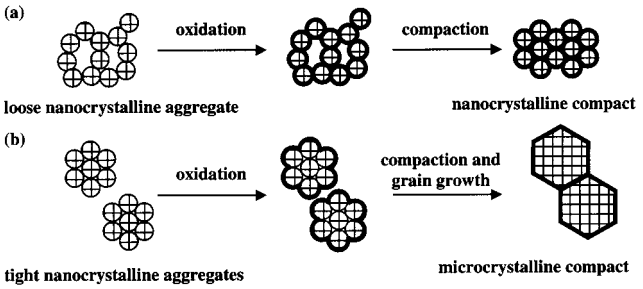

Figure 8. Scheme depicting proposed oxidation and consolidation behavior of *nano*-Al powders. Heavy black borders represent oxide coatings. (a) *nano*-Al prepared by gas condensation. (b) *nano*-Al prepared by chemical synthesis (present work).

Aluminum is extremely oxophilic. Surface oxidation occurs at O_2 partial pressures of $\geq 10^{-41}$ Torr,[45] which is exceeded under typical gas-condensation and mechanical-attrition conditions. The loose nanocrystallite aggregates formed by gas condensation[30,31,44] are susceptible to surface oxidation because a large surface area is exposed (Figure 8a). During mechanical attrition, low levels of adventitious O_2 and N_2 in the milling atmospheres often result in finely dispersed oxide and nitride impurity phases in Al and Al-containing intermetallics,[31,46,47] presumably because surface impurities are kneaded into the nanostructured aggregate particles. These impurities stabilize the nanocrystallites against grain growth during compaction and thermal treatments (Figure 8a).

The chemically prepared *nano*-Al is also adventitiously oxidized, but the extent and distribution of oxide impurities varies from the above. We propose the following rationale. The reducing reaction conditions prevent oxidation of nanocrystallite surfaces during chemical synthesis. Other likely oxidation-prevention factors are the small reactor (reaction-flask) volume and short preparation time in comparison to the other methods, which further limit exposure to adventitious oxygen. Tight aggregates precipitate from the solvent dispersion (Figure 5e, f, and h), in which the internal nanocrystallite interfaces are protected (Figure 8b). The dense aggregate structures contrast with the open, porous structures formed by gas condensation (Figure 8a).[30,31,44] Subsequent manipulation of the *nano*-Al after chemical synthesis allows adventitious oxidation of the external aggregate surfaces. Upon compaction, grains grow to sizes approaching the sizes of the initial aggregates (Figure 8b). Because most of the nanocrystallite surfaces in the chemically synthesized *nano*-Al remain unexposed and thus free of stabilizing oxide layers, the expected intrinsically rapid (room-temperature) grain growth is observed.

Conclusions

Chemical synthesis produces *nano*-Al having sufficient purity to exhibit intrinsically facile grain growth. Unlike chemical synthesis, gas-condensation and mechanical-attrition syntheses do not employ hydrocarbon solvents or heteroatom-containing reagents and, consequently, are not susceptible to impurities derived from them. However, these *nano*-Al syntheses employ processing methods and produce powder microstructures that

(42) Söhnel, O.; Garside, J. *Precipitation: Basic Principles and Industrial Applications*; Butterworth and Heinemann: Oxford, 1992; pp 163−180.
(43) Callister, W. D. *Mater. Sci. Engineering*, 3rd ed.; Wiley: New York, 1994; p 171.
(44) Sánchez-López, J. C.; González-Elipe, A. R.; Fernández, A. *J. Mater. Res.* **1998**, *13*, 703−710.
(45) Fujii, H.; Nakae, H.; Okada, K. *Acta Metall. Mater.* **1993**, *41*, 2963−2971.
(46) Suryanarayana, C.; Froes, F. H. *Adv. Mater.* **1993,** *5*, 96−106.
(47) Itsukaichi, T.; Masuyama, K.; Umemoto, M.; Okane, I.; Cabañas-Moreno, J. G. *J. Mater. Res.* **1993**, *8*, 1817−1828.

are inherently more prone to adventitious oxidation. The reducing reaction conditions and tightly packed aggregate microstructures achieved in the method-B chemical synthesis produce a lower oxide content and coarser oxide distribution than has been found in the *nano*-Al produced by the other methods.[31]

nano-Al prepared by gas condensation or mechanical attrition is extrinsically stabilized against grain growth by grain-boundary oxide impurities. Sánchez-López et al.[30] and Eckert et al.[31] independently established that oxide passivation of *nano*-Al prepared by these methods provides grain-size stability to temperatures far beyond expectation for pure *nano*-Al. We have now shown the corollary; reduction of oxide-impurity levels activates room-temperature grain growth, as predicted.[11,25] That narrower grain-size distributions may enhance stability[20] remains to be tested because such distributions are not practicably achievable by current methods. Barriers to grain growth in pure *nano*-Al having typical grain-size distributions are intrinsically low.

Metals having widely varying oxophilicities and other properties, that is, aluminum, copper,[3−8] silver,[3,4] palladium,[3,4] etc.,[11,25] are now known to exhibit low kinetic stabilities in nanocrystalline form. Consequently, low thermal stability should perhaps be a general expectation for *pure* nanocrystalline metals. Production of nanostructured materials with useful thermal properties will likely require nanocomposite strategies in which very finely dispersed second phases are purposefully incorporated to stabilize nanoscale grains.

Experimental Section

General Procedures and Starting Materials. All ambient-pressure synthetic manipulations were conducted under dry N_2 using standard inert-atmosphere techniques. Ground-glass joints were sealed with Teflon sleeves to minimize Si contamination of the products. Glow-discharge mass-spectrometric analyses were conducted by Shiva Technologies (Cicero, NY). X-ray diffraction procedures and data analysis are described in a separate section below.

Transmission electron microscopy (TEM) was performed on a JEOL 2000 FX instrument operating at 200 keV. Powder samples were prepared by combining 10−25 mg of powder with 10−30 mL of dry pyridine (under N_2). This mixture was then sonicated for 15−250 min in an ultrasonic cleaning bath until the powder was well suspended. Powders that were loosely agglomerated suspended immediately without sonication, whereas heavily aggregated powders required sonication for extended periods. While the suspension continued to be sonicated, a few drops were removed by syringe and placed on a holey-carbon-coated TEM grid in air. The grid was immediately placed into a tightly capped vial with 2−5 drops of the pyridine suspension and immediately loaded into the TEM antechamber while still wet with pyridine. This method proved quite effective at limiting oxidation, with many particles containing less than 10% oxygen.

The sample for TEM analysis from the consolidated pellet was prepared by cutting a thin slice from pellet B15-300 (see below) using a low-speed diamond wheel saw (South Bay Technology model 650) and an aqueous cooling solution (South Bay Technology P/N 0202460). The slice was then thinned by polishing on 1500-grit carborundum paper wet with MeOH and Ar-ion milled (Gatan dual ion mill model 600) at a 12° angle in a liquid-nitrogen-cooled specimen holder.

Scanning electron microscopy (SEM) was performed on a Hitachi S-4500 field-emission instrument. SEM specimens were prepared by dusting powders on carbon tape on Al stubs in the N_2 glovebox, sealing the stubs in tightly capped vials and performing SEM immediately after removing the vials from the glovebox. The stubs were removed from the vials and placed in the sample-exchange chamber immediately, keeping air exposure to less than one minute. Consolidated specimens were similarly examined before extended air exposure and/or after polishing as described below for microhardness testing.

Energy dispersive spectroscopy (EDS) with light-element detection was performed in conjunction with TEM and SEM using Noran Instruments Voyager II X-ray quantitative microanalysis system with digital imaging.

Vickers microhardnesses were measured on polished and/or unpolished pellet surfaces using a LECO M-400-H1 instrument with 50- and/or 100-g loads. The polished surfaces were prepared by successive polishing with 320, 600, 1000, and 2000 grit paper with flowing water, followed by lapping with 1.0 μm and 0.3 μm Al_2O_3 paste. Each hardness reported is the mean of 10 hardness measurements distributed over the entire surface of each pellet. Asymmetrical indentations were ignored.

Starting materials were obtained as follows. $LiAlH_4$ (95% purity, Aldrich) was used without further purification. NMe_2Et (99% purity, Aldrich) was distilled under nitrogen. $AlCl_3$ (Matheson, Coleman & Bell) was purified by a single sublimation from Al and NaCl. 1,3,5-trimethylbenzene (97%, Aldrich) was washed in a separatory funnel with concentrated H_2SO_4 until colorless, and then washed successively with deionized H_2O, 5% NaOH, and deionized H_2O. The 1,3,5-trimethylbenzene was then predried over CaH_2, distilled from sodium/potassium benzophenone ketyl and stored over type 4A sieves. Pentane was refluxed over sodium benzophenone ketyl with a few drops of tetraethylene glycol dimethyl ether (99+%, Aldrich), distilled, and stored over type 4A sieves. MeOH was refluxed over magnesium turnings activated with iodine, distilled, and stored over type 3A sieves. Pyridine (99.99%, Fisher) was refluxed over KOH for 4 days, distilled, and stored over type 4A sieves. Titanium(IV)isopropoxide (98% purity, Strem) was used as received.

N,*N*-dimethylethylamine alane, $H_3Al(NMe_2Et)$, was prepared by the method of Frigo et al.[40] **Warning: a powerful explosion occurred during the synthesis of $H_3Al(NMe_2Et)$.** The $AlCl_3/LiAlH_4$ slurry must be stirred thoroughly and rapidly to ensure initiation of the reaction upon slow addition of NMe_2Et. Failure to initiate leads to a mixture of exothermic-reaction partners in large, concentrated quantities, which is a dangerous situation prone to violent explosion. Complete details are given in the Supporting Information.

$H_3Al(NMe_2Et)$ is a colorless liquid that partially decomposed to a gray precipitate when stored at room temperature. When stored in liquid N_2 in an evacuated Schlenk flask, a cloudy white impurity developed, which settled upon standing at room temperature. In both cases, the decomposition was accompanied by a build-up of overpressure, which in one case fractured the top of the storage flask. $H_3Al(NMe_2Et)$ was usually repurified after several days of storage by recrystallization from pentane (−20 °C). The highest yields of *nano*-Al were obtained using freshly recrystallized $H_3Al(NMe_2Et)$.

Preparation of *nano*-Al. Method A. A stirred slurry of $AlCl_3$ (3.11 g, 23.3 mmol) and $LiAlH_4$ (2.66 g, 70.1 mmol) in 100 mL of 1,3,5-trimethylbenzene was refluxed for 16 h. The crude product (5.18 g, 94.5% yield) was collected on a glass frit, washed with two 10-mL portions of hexane, and dried in vacuo. The crude product was divided into three fractions (0.57, 2.24, and 2.43 g), which were washed with several portions of 0 °C MeOH (4−10 10-mL portions, respectively), dried in vacuo, and combined (overall yield of *nano*-Al: 2.24 g, 83.0 mmol, 89% with respect to $AlCl_3$). Elemental analysis of method-A *nano*-Al was conducted on a consolidated pellet (see below).

Preparation of *nano*-Al. Method B. The decomposition of $H_3Al(NMe_2Et)$ was performed using a range of molar ratios of decomposition catalyst, Ti(O-*i*-Pr)$_4$, on a variety of reaction scales using several different batches of $H_3Al(NMe_2Et)$ (see Table 1).

In general, 25 to 100 mL of $H_3Al(NMe_2Et)$ and 75 to 300 mL of 1,3,5-trimethylbenzene (approximately 2.5 mol of $H_3Al(NMe_2Et)$/L of 1,3,5-trimethylbenzene) were placed in a Schlenk flask. Then Ti(O-*i*-Pr)$_4$ ($0-1.2 \times 10^{-2}$ moles per mole of $H_3Al(NMe_2Et)$) was added to the room-temperature solution. The clear, colorless solution turned tan to dark brown, depending upon the amount of added Ti(O-*i*-Pr)$_4$, and fumed. In the runs using the Ti(O-*i*-Pr)$_4$ catalyst, rapid gas evolution ensued when the solution was warmed to reflux (ca. ≤100 °C). Gas evolution was complete within 15 min. and heating was continued for an additional ≥20 min. In the runs without the Ti(O-*i*-Pr)$_4$ catalyst, complete decomposition required several h at higher reflux temperatures (≈164 °C). Powders or spongy deposits of *nano*-

Al were then precipitated with or without catalyst, respectively. The coarseness of the powder depended upon the amount of catalyst used (see Results); in some cases, the product was so fine it passed in part or entirely through a medium porosity glass frit. The spongy product produced without catalyst or the collected powders were washed with hexane or pentane and dried in vacuo. The isolated *nano*-Al yields (with respect to starting $AlCl_3$) ranged from 28 to 83% for uncatalyzed runs and to 60−99% for Ti(O-*i*-Pr)$_4$-catalyzed runs. Elemental analysis of method-B *nano*-Al was conducted on a consolidated pellet (see below).

Consolidation of *nano*-Al. Pellets 13 mm in diameter and 2 to 12 mm in thickness were pressed from the *nano*-Al produced by methods A and B using a uniaxial hot press in an Ar-filled glovebox. The press employed TZM (a molybdenum-based alloy) plungers and die with a disposable graphite sleeve for lubrication and ease of pellet removal. All pellets (0.75−3.53 g) were pressed at 350 MPa for 1 h at room temperature, 100 °C, or 300 °C. The pellets were labeled A-100−B15-300 to specify the source of the powder and the pressing temperature (see Tables 1 and 2 and the Results).

Elemental analysis by glow-discharge mass spectrometry gave the following results. The major impurities in sample A-300 were (wt %): C, 3.00; N, 0.19; O, 4.00; Si, 0.24; Cl, 3.30; K, 2.10; Li, 0.12; Al, 87.0 (by difference). The minor impurities were (ppm by wt): B, 190; Na, 280; Mg, 28; S, 14; Ca, 2.3; Ti, 11; V, 0.19; Cr, 30; Mn, 2.5; Fe, 90; Ni, 27; Cu, 6; Zn, 8.6; In, 73; Ta, <28; W, 0.12.

The major impurities in B13-100 were (wt %): C, 0.23; O, 0.25; N, 0.055; Cl, 0.14; Ti, 0.32; and Al, 99.0 (by difference). The minor impurities were (ppm by wt): Li, 1.3; B, 0.15; F, <0.05, Na, 2.9; Mg, 0.37; Si, 40; S, 1.8; K, 4.8; Ca, 0.61; Cr, 0.5; Mn, 0.01; Fe, 1.5; Ni, 0.35; Cu, 0.4; Zn, 0.27; Ga, 0.12; Mo, 0.9; In, 1.9; Ta, <1; W, 0.05.

X-ray Diffraction (XRD) Procedures and Data Analysis. XRD patterns were obtained using a Rigaku vertical powder diffractometer with Cu Kα ($\lambda = 1.541\,845$ Å) radiation and Materials Data Inc. (MDI) automation and software. All XRD patterns were collected in a high-resolution configuration with a 0.040°-2θ step and a 1-second count. The XRD samples (1.5 × 2 cm smear mounts) were prepared in a N_2-filled glovebox and coated with a thin film of polyvinyltoluene (PVT) to minimize air exposure. The PVT film was applied by dripping a toluene solution of PVT onto the prepared XRD slide and evaporating it to dryness. XRD line widths were determined using the MDI software to electronically subtract the background and Kα2 peaks. A background level was drawn across each peak, which the software integrated to determine the integral breadth (which the software terms fwhm) by dividing the area by the peak height. The instrumental broadening was determined by collecting a pattern of the NIST Standard Reference Material (SRM) 660, (LaB_6), using a step of 0.020° 2θ, with a 1-second count. In subsequent calculations, see below, the fwhm of the SRM 660 peak closest to the experimental peak was used as the instrumental broadening.

In the high-resolution configuration we employed, the instrumental broadening and size-distribution broadening of the XRD reflection profiles are better approximated by Cauchy (or Lorentzian) peak shapes than by Gaussian peak shapes.[48] Therefore, Cauchy peak shapes were assumed, and the intrinsic breadth was extracted using $B = \beta + b$, where B is the experimental (observed) breadth, β is the intrinsic breadth in the sample, and b is the instrumental breadth.[48] This method resulted in narrower intrinsic peak widths and hence larger apparent coherence lengths than were obtained when Gaussian peak shapes were assumed. Because the experimental peak shapes had a small Gaussian component, the mean coherence lengths obtained from the pure Cauchy analysis were overestimates; however, these coherence lengths were more consistent with TEM and SEM particle sizes than were those calculated assuming pure Gaussian peak shapes ($B^2 = \beta^2 + b^2$).[48]

(48) Klug, H. P.; Alexander, L. E. *X-ray Diffraction Procedures for Polycrystalline and Amorphous Materials*, 2nd ed.; Wiley-Interscience: New York, 1974, Ch. 9.

The mean coherence lengths (crystallite sizes) in the as-precipitated powders were calculated using the Scherrer formula $L = (1.0\lambda)/(\beta \cos \theta)$,[48] where λ is the X-ray wavelength in nm, β is the intrinsic peak width in radians (2θ), θ is the Bragg angle, and 1.0 is the Scherrer constant. This calculation assumed that the *nano*-Al powders were strain-free, which was supported by subjecting the data to the size-strain deconvolution process described below. The sizes determined from the deconvolution calculations were within error limits of the values determined from the Scherrer formula, and the strain values were small (10^{-4}) and both positive and negative. Thus, strain was negligible. The errors in the mean coherence lengths (sizes) were estimated from the variation in coherence length calculated from the 111, 200, 220, 311, and, when collected, the 222 diffraction intensities and do not include the systematic error introduced by assuming pure Cauchy peak shapes. Note that, as the intrinsic broadening increases, the assumptions about line shape become less important. These results are recorded in Table 1.

Both size and strain broadening contributed to the intrinsic peak widths of the consolidated pellets. The broadening due to crystallite size, $(\delta s)_{size}$, (where $s = 2 \sin \theta/\lambda$) is independent of s, whereas the strain broadening, $(\delta s)_{strain}$, is proportional to s.[32] Thus, the dependence of the corrected peak width $(\delta s)_0$ on s enables the separation of size and strain broadening. The broadening due to particle size is best approximated by a Cauchy function, whereas the broadening due to strain is best approximated by a Gaussian function.[32,48] The contributions of size and strain broadening were separated following Eckert et al.[32] who substituted the functional dependence of $(\delta s)_{size}$ and $(\delta s)_{strain}$ on s into an approximation for a Cauchy/Gaussian convolution to obtain eq 3

$$\frac{1}{(\delta s)_0} \approx d - 6.25\langle e^2 \rangle\, d\left[\frac{s}{(\delta s)_0}\right]^2 \qquad (3)$$

where d is the volume-averaged grain size, and $\langle e^2 \rangle^{1/2}$ is the rms microstrain. The parameters d and $\langle e^2 \rangle^{1/2}$ were determined from the linear least-squares fit of $1/(\delta s)_0$ vs $[s/(\delta s)_0]^2$ from all of the diffraction peaks collected from the sample, whereas the error in the fit estimated the error in these parameters. The results are recorded in Table 2.

The values obtained for the grain size and rms strain have large uncertainties for two reasons. (1) For large crystallite sizes, the intrinsic peak broadening approaches the error in the measurement. (2) The powders and pellets contained a complex distribution of particle shapes, which varied from sample to sample. The breadth of XRD reflections is also influenced by particle shape. Shape anisotropy variously broadens lines corresponding to different crystallographic directions within the crystallites. We were unable to account for this shape effect in our analysis.

Acknowledgment. This work was funded by NSF grants CHE-9158369 and CHE-9709104, with additional support from the Exxon Education Foundation, Emerson Electric, Monsanto, and Eastman Kodak. J.A.H. was partially supported by a Department of Education GAANN grant (P200A40147). We thank Nilesh V. Gunda for assistance with pressing and microhardness testing, and W. L. Gladfelter for suggesting the use of the Ti(O-*i*-Pr)$_4$ catalyst. We also thank S. Hariprasad for advice on polishing pellets and making microhardness measurements, and P. C. Gibbons, K. F. Kelton, and J. A. Hollingsworth for helpful discussions.

Supporting Information Available: Precautions for the preparation of $H_3Al(NMe_2Et)$ (2 pages, print/PDF). See any current masthead page for ordering information and Web access instructions.

JA981972Y